ULX pulsar Swift J0243.6+6124 observations with *NuSTAR*: phase-resolved spectroscopy and the variability of the Iron line

ABSTRACT

Key words: pulsars: individual: Swift J0243.6+6124 – X-rays: binaries

1 INTRODUCTION

The X-ray transient Swift J0243.6+6124 was discovered in its outburst by *Swift* Burst Alert Telescope (BAT) in the 15–50 keV energy range in the end of 2017 (Cenko et al. 2017). Pulsations with period of about 9.8 sec were detected later in 0.3–10 keV range (Kennea et al. 2017), establishing the source as an accreting neutron star and transient X-ray pulsar. Its orbital parameters were established for the first time with *Fermi* Gamma-Burst monitor (GBM) in Jenke et al. (2018); Doroshenko et al. (2018) and were refined since. The 2017-2018 outburst lasted approximately 200 days, after which the source transitioned to the regime of flaring activity. During the outburst of the source several dedicated observational campaigns were performed in radio, optical and X-ray wavelengths. The optical counterpart turns out to be a Be-class star (Kouroubatzakis et al. 2017; Bikmaev et al. 2017; Reig et al. 2020), thus classifying the source as a Be X-ray binary (BeXRB). The distance to the source is estimated to be $6.8^{+1.5}_{-1.1}$ kpc according to *Gaia* data (Bailer-Jones et al. 2018), and 5.5 ± 1.7 kpc from the dedicated optical observations (Reig et al. 2020). With the distance information, the luminosity of the pulsar was calculated in a peak of the outburst and found to be larger than Eddington luminosity for a neutron star (Tsygankov et al. 2018; Doroshenko et al. 2020). Such high luminosity places the source in a cohort of Ultra-Luminous Pulsars (ULP), and the first of this kind to be found in our galaxy. Radio observations revealed the presence of strong emission and its variability, indicating the presence of radio jets with varying intensity (van den Eijnden et al. 2018, 2019a).

X-ray studies of this pulsar are numerous. In particular, Jaisawal et al. (2018) performed the first spectroscopy and timing analysis of the X-ray emission with the help of *NuSTAR* observatory. They found the pulse profile which depends on the energy of the photons, and detected the spectral shape changing with the rotation of the neutron star. Such behaviour is typical for transient X-ray pulsars. Doroshenko et al. (2018) performed the analysis of the rotation frequency changes and concluded that the source accretes from the disc, and provide the first orbital parameters. A study by Wilson-Hodge et al. (2018) used the information from *Fermi*/GBM and *NICER* telescopes to investigate the spectral and timing behaviour of the Swift J0243.6+6124. From the timing analysis they discover the quasi-periodic oscillations at frequency ∼ 50 mHz and changing broadband variability. Pulse profiles show strong evolution and energy dependence with transitions from single- to double-peaked shape (and vice-versa) as

the pulsar brightens (fades). From the luminosity of the pulse profile transition (connected with the change in the accretion regime) they estimate the magnetic field of the pulsar to be $B > 10^{13}$ G. On the other hand, Tsygankov et al. (2018) argue that the magnetic field should be smaller based of the absence of the propeller effect onset at the declining phase of the outburst. Tao et al. (2019) analysed the spectra of a few *NuSTAR* observations and show that the spectra an be described with a smooth continuum and several black-body components associated with different emission regions. The properties of the emission component change between sub- and super-Eddington regimes of the object.

Insight-HXMT provided fruitful broadband X-ray data with high cadence. For instance, Zhang et al. (2019) analyzed the wide energy range and found that the evolution of pulsed fraction in time is different between different energy bands. Broadband spectral analysis (2–150 keV) reveals no trace of cyclotron scattering absorption feature. Similar conclusions are derived from *AstroSat* data in Beri et al. (2021). Doroshenko et al. (2020) reported about the changes in timing and spectral properties of Swift J0243.6+6124 based on these data. It was interpreted as the onset of super-Eddington accretion via the gas pressure dominated disc, GPD (first transition), and the transition of GPD to radiation pressure supported disk (RPD, second transition). These results are important since they show that not only radiation patterns change with pulsar luminosity, but also the accretion geometry may evolve in the course of the outburst. The presence of RPD indicate that the magnetic field may not be very large. Kong et al. (2020) used the same *Insight-HXMT* to study the spectral transition sequence of the pulsar, including the changes in thermal component and spectral hardness. The spectral evolution indicate drastic changes in the angular distribution of escaping radiation. Wang et al. (2020) studied the timing properties of the source and its dependence on the luminosity, especially with pulsation shapes recorded on the similar luminosity but different outburst phase.

Chandra spectroscopy of absorption lines indicate the possible fast outflows of the material (blue-shift of Ne and Mg ∼ 0.22*c*), but can also be interpreted as Fe lines at rest (van den Eijnden et al. 2019b). The iron line complex was studied elaborately in the work of Jaisawal et al. (2019) with *NICER* and *NuSTAR*. They detected strong luminosity-dependent and broad emission lines in 6–7 keV range with possible asymmetric and shifted shapes due to the redshift effects. The complex consists of emission at 6.4, 6.7 and 6.98 keV from neutral and ionized iron atoms, and the neutral line is very broad

(σ up to 1 keV).They interpret the results in such way that the Iron emission is produced far from the pulsar (in a disc or plasma in the magnetosphere).

In none of the works above the CSRF was found in the X-ray band. But in the work by Sugizaki et al. (2020) it is reported that the particular spectral feature found by MAXI GSC monitor may be explained by the absorption at $\sim$ 10 keV, implying the magnetic field of a few 10^{12} G. Indirect methods provide only upper or lower limits for the magnitude of the magnetic field and may contradict each other (see above).

Notwithstanding ample observational data, only one phase-resolved spectroscopic study was done with *NuSTAR* data in the low state of the pulsar (Jaisawal et al. 2018). This paper aims to fill this gap and is dedicated to phase-resolved spectroscopy of available *NuSTAR* observations, with particular emphasis on the variability of Iron line complex. In section 2 we describe the data reduction and analysis. In sect. 3.1 we discuss the timing analysis, in 3.2.1 we describe the results of phase-averaged spectra, and in 3.2.2 we report on the phase-resolved spectroscopy. We discuss our results in sect. 4 and conclude in sect. 5. In our paper we assume the distance to the source 6.8 kpc and isotropic luminosity.

2 *NuSTAR* DATA

NuSTAR (Harrison et al. 2013) is a hard X-ray focusing observatory sensitive in 3-79 keV energy range with energy resolution 4% at 10 keV. It has two identical detectors (modules): FPMA and FPMB. Data from each is reduced separately. In 2017-2018 type II outburst, the system Swift J0243.6+6124 was observed with *NuSTAR* satellite five times between MJD 58000 and MJD 58200 (observations 9030231900(2,4,6,8), 90401308001). Observation 90401308001 was excluded due to its short exposure. We add observation 90401308002 of the one of the subsequent mini-outburst (likely Type I outburst of BeXRB) to our data set. We use thee following aliases for observations: 90302319002 – I, 90302319004 – II, 90302319006 – III, 90302319008 – IV, 90401308001 – V.

The *NuSTAR* observatory data reduction was carried out using the `HEASOFT` v. 6.28 package and latest *NuSTAR* CALDB files. Standard data-processing tools were used to extract level 2 (`nupipeline`) and 3 (`nuproducts`) data FPMA and FPMB modules. We choose source and background regions for data extraction (separately for FPMA and FPMB): the former was centred on the source position, while the latter was placed as far from the source as possible (in the opposite CCD chip). Both regions had a circular shape with 180 arcsec radius. Due to the high count rate, for all observations we set status expression flag on the value "STATUS==b0000xxx00xxxx000" as recommended[1]. All data were barycentred, but the time of arrival of photons was not corrected for orbital motion of the system due to the lack of orbital solution based on all gathered data about the source. Due to the relatively short on-source time of *NuSTAR* observations (a few tens of ks) compared to the orbital period of $\sim$ 30 days this should not present any errors in the timing analysis. Spectra from both modules were simultaneously fit between 4 and 79 keV with `Xspec` package (Arnaud 1996). In phase-resolved spectroscopy photons were folded into 10 phase bins. All *NuSTAR* spectra photons were grouped to have at least 25 counts per energy bin and χ^2 statistics used. The confidence intervals are given for 68% probability.

3 RESULTS

3.1 Timing analysis

Fig. 1 shows the light curve of the source in the 15–50 keV band (*Swift*/BAT data[2]) and the 0.3–10 keV range (*Swift*/XRT data[3]) in arbitrary units of count rate. In both bands the outburst had a bell shape with rise and fall timescales shorter in XRT band. The main, giant outburst lasted approx 200 days, and was followed by a series of smaller flares (possible Type I outbursts). Dates of *NuSTAR* observations are marked at vertical lines. All observations except one are taken during the main outburst (I–IV, from left to right), and one during the smaller flare (V, right-most in the figure). Observations I and V are in the 'low' state, and observations II, III and IV are in 'high' state.

Pulsations of X-ray flux were detected in all observations. We assigned the period of the pulsar in a given observations with `EFSEARCH` routine from the combined light curve of *NuSTAR* detectors. The barycentred periods (in seconds) are 9.85425, 9.84435, 9.82340, 9.80105, 9.7918 for observations I, II, III, IV and V respectively. The periods were used for folding times in pulse profiles and phase-resolved spectroscopy. No phase connection was made to synchronize pulse profiles from different observations.

In Fig. 2 we show the pulse profiles in the 4–79 keV energy range of all five *NuSTAR* observations. Pulse profile is defined as the mean count rate in a particular phase bin divided by the overall average count rate of the source. In the beginning of the outburst (observation I, 90302319002) the pulse profile had a complex shape with multiple minor peaks, but overall the profile is dominated by the two-peaked component with unequal maxima. The last observation (II, 90401334002) taken during another flare of the source, but in similar brightness, shows very similar but somewhat smoother shape. The pulsed fraction [4] was $\sim$ 30% in this energy range.

As the source becomes more luminous, the pulse profile changed drastically. In two brightest observations (II and III) the pulse profile showed a very smooth and symmetric double-peaked shape. In the former observation the peaks were roughly equal in amplitude and the pulsed fraction was 45%, whilst in the latter one peak clearly dominated the overall shape and the pulse profile was slightly larger, 55%. In the next observation, IV, the pulse profile featured two asymmetric peaks of roughly equal height. The fraction of pulsed emission was $\sim$ 30%.

3.2 Spectral analysis

3.2.1 Phase-averaged spectra

The broadband spectrum of the source in the energy range 4–79 keV has a shape typical for transient X-ray pulsars (Filippova et al. 2005) and was extensively analysed in the works cited in sect. 1. The spectrum has a shape similar to that of power law with exponential cutoff, a strong Iron emission feature, lacks cyclotron absorption line and has thermal components (Jaisawal et al. 2018; Tao et al. 2019; Jaisawal et al. 2019; Kong et al. 2020).

We use the following `Xspec` formula to describe the emission of the pulsar based on *NuSTAR* data: `phabs*[gauss+gauss+edge*(cutoffpl + bbodyrad)]`.

---

[1] https://heasarc.gsfc.nasa.gov/docs/nustar/analysis/

[2] https://swift.gsfc.nasa.gov/results/transients/weak/SwiftJ0243.6p6124/

[3] reduced from online tool https://www.swift.ac.uk/user_objects/, see (Evans et al. 2007)

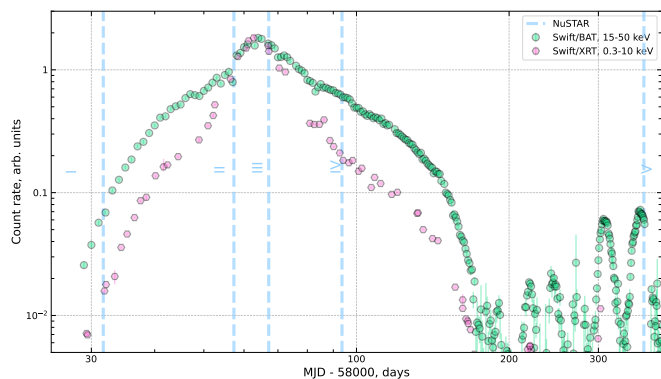[4] defined as $\frac{\max C - \min C}{\max C + \min C}$ of the pulse profile C

Figure 1. *Swift*/BAT and XRT light curves of a source in arbitrary units of count rate (orange and blue symbols). *NuSTAR* observations are marked with pink vertical lines. Note the time axis in log scale in units of days after MJD 58000.
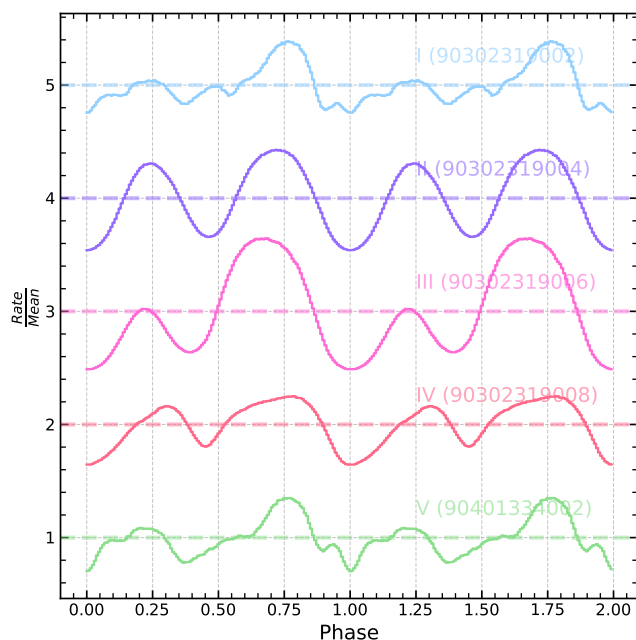

Figure 2. Pulse profiles (normalized to mean count rate) of *NuSTAR* observations in the 4–79 keV energy range. The profiles were offset from each other for readability. The time since the start of the outburst goes from the bottom to the top. All pulse profiles except for the first and the last were taken in super-Eddington state of the pulsar. Profiles were shifted so that the main minimum is at phase 0.

`phabs` takes care for the interstellar absorption in the direction of the source[5] and has optical depth fixed at 0.8×10^{22} cm^{-2}. `gauss` plays a role of emission lines of Iron. The two lines have energies fixed at 6.4 and 6.67 keV, and the latter has also its width fixed at 0.05 keV, all according to analysis of *NICER* spectra Jaisawal et al. (2019, table 1). Note that the third gaussian at energy 6.98 but with a very small amplitude is not resolved by *NuSTAR*. Note that possible asymmetry of the Iron line is mentioned in Tao et al. (2019); Jaisawal

et al. (2019). `edge` is a component responsible for modelling of the absorption edge of Iron K-α and has a prominent optical depth of ~ 0.1 according to *NICER* and *NuSTAR* spectra (Jaisawal et al. 2019), and we fix its energy at 7.1 keV. The second gaussian and the edge component were not added to the spectra of observations I and V (i.e. low-state).

`cutoffpl` and `bbodyrad` are for continuum components and thermal radiation respectively, with no restrictions and fixed parameters. Cross-calibration constant is added between FPMA and FPMB spectra. We tried to use different model for continuum, comptonization model `compTT`, which failed to describe all spectra except for two brightest observation (II and III). Table 1 show the parameters of the spectra in all observations for our `cutoffpl` continuum model. The results are presented in the appendix.

In the low state observations, I and V, the spectral parameters are similar, especially of the iron line and thermal black body component. The equivalent width of the iron line was ~ 80 eV and the hump width (σ) ~ 0.45 keV. The black body temperature was ~ 3 keV. Note that the parameters of the spectra are consistent to those in Jaisawal et al. (2018, table 1) for their 'Cutoff+BB' model. In fig. 3 panel (a), we show the spectral data from both observations and residuals to the fiducial model in both detectors. Residuals are large at high energies and it may be attributed to the imperfect knowledge of the pulsar spectra shape.

In the two brightest, II and III the spectra is somewhat softer than in low state and with smaller cutoff energies. Black body temperatures are around 1 keV, lower than in the low state, and with larger normalisation. Emission line at 6.4 keV is very broad (σ ~ 1.8 keV) and with very large equivalent width around 1 keV. The iron K-edge has a depth around 12-17%. The parameters of spectral components in observation II are consistent with the results of joint *NuSTAR* and *NICER* spectra from Jaisawal et al. (2019, table 1). Observation IV has the hardest observed, with smaller iron equivalent width (~ 0.8 keV) and its energy width σ ~ 1.8 keV. In fig. 3 we show the spectra and residuals for the three observations. The edge optical depth is 0.129.

Minor discrepancy between out model and the data are seen near the iron line (6–7 keV region). It may be attributed to the reported asymmetry of the iron line (Tao et al. 2019; Jaisawal et al. 2019), or to the simple model of continuum and/or edge component. We decided to not model the residuals further since its effect is limited, especially in phase-resolved spectra. The results of phase-averaged spectra suggest drastic changes in the emission properties of the pulsar, especially in the evolution of the Iron complex and possible thermal component. In the next section we perform the similar analysis but for phase-resolved energy spectra.

3.2.2 Phase-resolved spectra

We study the evolution of spectral parameters as the function of rotation phase of the neutron star. The pulse was divided into 10 phase bins with equal width, and the spectra was extracted for both detectors as described in 2. We fit the spectra with the same model as for the phase-averaged case, but we fix the energy width of the first Gaussian (6.4 keV) to its values found in the phase-averaged spectra of the corresponding observation. For observations II, III and IV we also fix the amplitude of the second gaussian because this component is insignificant in phase-resolved spectra with ~ 10 times smaller photon count than in its phase-averaged counterpart. The results within two groups of observation, low and high state, are very similar. However, the difference in spectral variability between two groups is large as described below.

comp	par	ObsID 90302319002	90302319004	90302319006	90302319008	90401334002
constant	factor	1.011 ± 0.001	0.999 ± 0.001	0.992 ± 0.001	0.999 ± 0.001	1.017 ± 0.001
phabs	nH	0.800(fix)	0.800(fix)	0.800(fix)	0.800(fix)	0.800(fix)
cutoffpl	HighECut	$23.777^{+0.491}_{-0.476}$	$20.235^{+0.270}_{-0.269}$	$20.028^{+0.339}_{-0.333}$	$17.154^{+0.124}_{-0.123}$	$22.884^{+0.325}_{-0.320}$
	PhoIndex	1.090 ± 0.013	1.276 ± 0.015	$1.361^{+0.020}_{-0.021}$	$0.754^{+0.009}_{-0.010}$	1.023 ± 0.010
	norm	0.274 ± 0.005	$10.350^{+0.329}_{-0.328}$	$19.425^{+0.867}_{-0.852}$	1.559 ± 0.031	0.225 ± 0.003
bbodyrad	kT	3.039 ± 0.019	0.873 ± 0.017	$1.129^{+0.034}_{-0.038}$	$0.746^{+0.016}_{-0.015}$	2.947 ± 0.016
	norm	$2.029^{+0.036}_{-0.035}$	$3999.783^{+342.087}_{-314.664}$	$1110.420^{+114.685}_{-97.425}$	$2082.393^{+238.509}_{-210.838}$	$1.803^{+0.029}_{-0.028}$
gaussian	LineE	6.400(fix)	6.400(fix)	6.400(fix)	6.400(fix)	6.400(fix)
	Sigma	$0.463^{+0.046}_{-0.043}$	1.764 ± 0.012	$1.690^{+0.018}_{-0.019}$	1.755 ± 0.018	$0.428^{+0.028}_{-0.027}$
	eqw	$0.076^{+0.007}_{-0.006}$	$1.221^{+0.059}_{-0.049}$	$0.906^{+0.083}_{-0.063}$	$0.835^{+0.036}_{-0.040}$	0.076 ± 0.005
	norm	0.003 ± 0.000	$1.034^{+0.026}_{-0.027}$	$1.208^{+0.058}_{-0.057}$	0.240 ± 0.006	0.003 ± 0.000
gaussian$_4$	LineE	-	6.670(fix)	6.670(fix)	6.670(fix)	-
	Sigma	-	0.050(fix)	0.050(fix)	0.050(fix)	-
	norm	-	0.013 ± 0.002	0.019 ± 0.003	0.001 ± 0.000	-
edge	MaxTau	-	0.171 ± 0.008	0.123 ± 0.008	0.129 ± 0.006	-
	edgeE	-	7.100(fix)	7.100(fix)	7.100(fix)	-
stat	chi2	2490.54/2293	2658.69/2309	2332.99/2170	3378.30/2735	2918.18/2699

Table 1. Spectral parameters of *NuSTAR* spectra of Swift J0243.6+6124 in its 2017-2018 outburst. The spectral model is described in sect. 3.2.1: `phabs*[gauss+gauss+edge*(cutoffpl + bbodyrad)]`
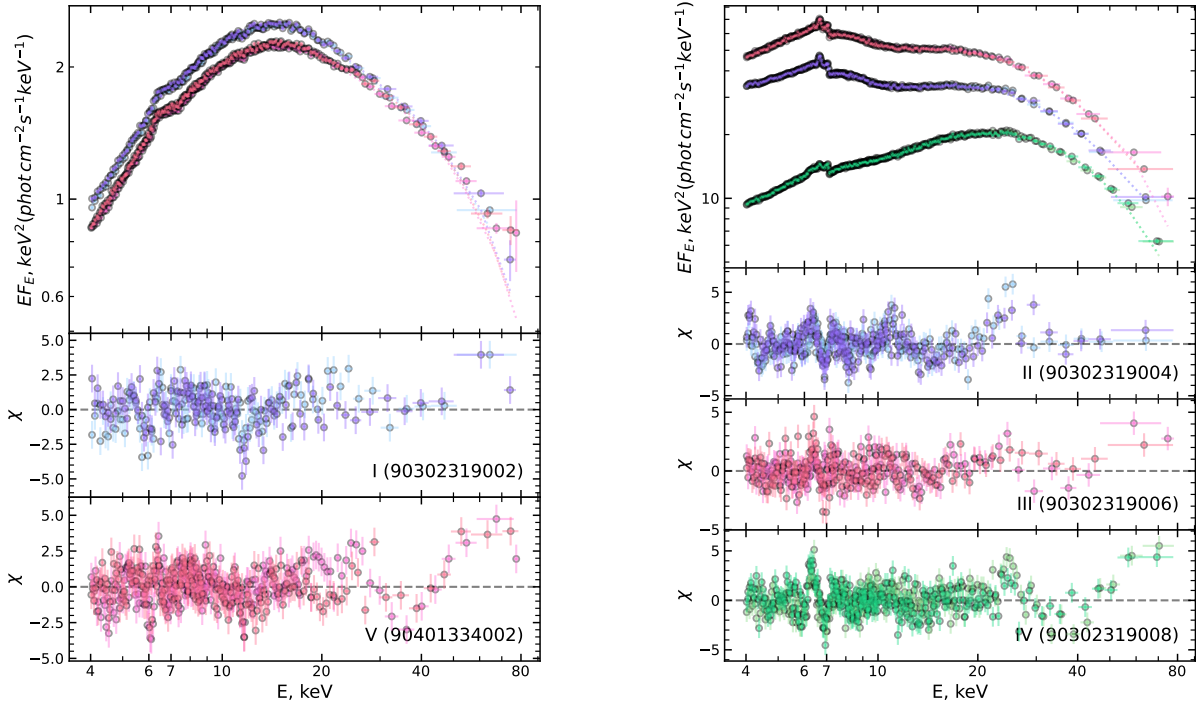
(a) Low state, observations I and V

(b) High state, observations II, III and IV

Figure 3. Unfolded spectra of the source and its model. Top subplots show the unfolded spectra from FPMA and FPMB by colored circles, and the dotted line represents the best-fitting approximation. Lower subplots show the respective residuals from the model. Panel (a) illustrates the low state observations, panel (b) - high state.

The representative results are presented In Fig. 4. In general case, the parameters are following (from top to bottom subplot): pulse profile of the count rate in the 4-79 keV energy range for each individual phase bin, together constituting the total pulse profile; 6.4 keV Gaussian equivalent width in keV; K-edge optical depth; 6.4 keV Gaussian normalisation; Photon index of the continuum; e-folding energy of the continuum; black body inferred temperature; black body inferred normalization. Two full rotations are shown, and the phase bin ranges are of different colors.

In panel (a) of Fig. 4 we show the parameters of spectra of observation I, the low state. The pulse profile is the same as described in sect. 3.1. The equivalent width of the Iron show some variations without particular shape, as does the normalization of the line. The photon index and the cutoff energy change significantly as the neutron star rotate. The black body temperature stays approximately constant in all phase bins but dips in three consecutive bins before the main maxima of the pulse profile. The normalisation of the thermal component is anti-correlated with its temperature, so it peaks then the temperature drops. The changes in the continuum and thermal components are hard to interpreter because those components are phenomenological and the parameters adjust itself for the very complex changes in the spectral energy distribution of the radiation of thee pulsar. The spectra evolution is consistent with the report of Jaisawal et al. (2018) who analysed the same observation. In the last observation, V (low state), the spectral variability are very similar and presented in appendix A, panel (c) of Fig. A1. The main difference is that there is a essential drop in the iron line flux in one phase bin while the spectra is suddenly becomes harder than average.

In panel (b) of Fig. 4 we show the parameters of spectra of observation II, the high state. The equivalent width and the K-edge optical depth show strong periodic variability: the equivalent width pulsates between roughly 0.5 and 1.7 keV, and the edge between 0.1 and 0.4. Both edge and equivalent width are anti-correlated with the count rate. The normalisation of the iron line show small level of variability without particular shape. The parameters of power law continuum show variations typical for X-ray pulsars. The black body component fluctuates in temperature and normalisation approximately in phase with the count rate but with smaller amplitude. Observations III and IV show very similar pattern, see panels (a,b) of Fig. A1. Observation IV, however, has different profile of flux, and its variations of Iron line follow slightly different trend than in other high state observations.

The striking variability of the iron complex (iron line equivalent width and the optical depth of the edge) is evident in the high state. Since a phenomenological model is used for the continuum, we plot the model-independent ratio between the spectra of a specific bin and the `cutoffpl+bbodyrad` model for continuum for a given observation. For example, bottom panel in Fig. 5 shows the ratio of phase-resolved spectra in bins 2 and 4 (phases 0.1-0.2 and 0.4-0.5) of observation II to the `cutoffpl+bbodyrad` model with parameters from the second row of Table 1. Bin 2 is the local minimum of iron line equivalent width and the edge depth, whilst bin 4 is a respective maximum (panel (b) of Fig. 4). In the ratio plot one sees that the Iron line is indeed higher in amplitude for bin 4, whilst the depression of the spectrum after 7.1 keV is smaller in bin 2. In the top panel of the figure, it can be seen that the difference in continuum in bins 1 and 2 of Observation I dominates the spectrum variability (from panel (a) of Fig. 4 one sees that the black body parameters differ significantly from bin 1 and bin 2). For observations III, IV and V the results are presented in Fig. A2 in the appendix, and the behaviour of the spectra is similar within luminosity states.

# 4 DISCUSSION

5 CONCLUSION

DATA AVAILABILITY STATEMENT

We are grateful for the *NuSTAR* data to the High Energy Astrophysics Science Archive Research Center (HEASARC) Online Service [6] provided by the NASA/Goddard Space Flight Center. To download data of *NuSTAR* used in this work, one should use observations ID from sect. 2. *Swift* data for light curves are available from the links in sect. 3.1.

REFERENCES

Arnaud K. A., 1996, in Jacoby G. H., Barnes J., eds, Astronomical Society of the Pacific Conference Series Vol. 101, Astronomical Data Analysis Software and Systems V. p. 17
Bailer-Jones C. A. L., Rybizki J., Fouesneau M., Mantelet G., Andrae R., 2018, AJ, 156, 58
Beri A., et al., 2021, MNRAS, 500, 565
Bikmaev I., et al., 2017, The Astronomer's Telegram, 10968, 1
Cenko S. B., et al., 2017, GRB Coordinates Network, 21960, 1
Doroshenko V., Tsygankov S., Santangelo A., 2018, A&A, 613, A19
Doroshenko V., et al., 2020, MNRAS, 491, 1857
Evans P. A., et al., 2007, A&A, 469, 379
Filippova E. V., Tsygankov S. S., Lutovinov A. A., Sunyaev R. A., 2005, Astronomy Letters, 31, 729
HI4PI Collaboration et al., 2016, A&A, 594, A116
Harrison F. A., et al., 2013, ApJ, 770, 103
Jaisawal G. K., Naik S., Chenevez J., 2018, MNRAS, 474, 4432
Jaisawal G. K., et al., 2019, ApJ, 885, 18
Jenke P., Wilson-Hodge C. A., Malacaria C., 2018, The Astronomer's Telegram, 11280, 1
Kennea J. A., Lien A. Y., Krimm H. A., Cenko S. B., Siegel M. H., 2017, The Astronomer's Telegram, 10809, 1
Kong L. D., et al., 2020, ApJ, 902, 18
Kouroubatzakis K., Reig P., Andrews J.,) A. Z., 2017, The Astronomer's Telegram, 10822, 1
Reig P., Fabregat J., Alfonso-Garzón J., 2020, A&A, 640, A35
Sugizaki M., Oeda M., Kawai N., Mihara T., Makishima K., Nakajima M., 2020, ApJ, 896, 124
Tao L., Feng H., Zhang S., Bu Q., Zhang S., Qu J., Zhang Y., 2019, ApJ, 873, 19
Tsygankov S. S., Doroshenko V., Mushtukov A. A., Lutovinov A. A., Poutanen J., 2018, MNRAS, 479, L134
Wang P. J., et al., 2020, MNRAS, 497, 5498
Wilson-Hodge C. A., et al., 2018, ApJ, 863, 9
Zhang Y., et al., 2019, ApJ, 879, 61
van den Eijnden J., Degenaar N., Russell T. D., Wijnands R., Miller-Jones J. C. A., Sivakoff G. R., Hernández Santisteban J. V., 2018, Nature, 562, 233
van den Eijnden J., Degenaar N., Russell T. D., Hernández Santisteban J. V., Wijnands R., Miller-Jones J. C. A., Rouco Escorial A., Sivakoff G. R., 2019a, MNRAS, 483, 4628
van den Eijnden J., et al., 2019b, MNRAS, 487, 4355

[6] https://heasarc.gsfc.nasa.gov/cgi-bin/W3Browse/w3browse.pl
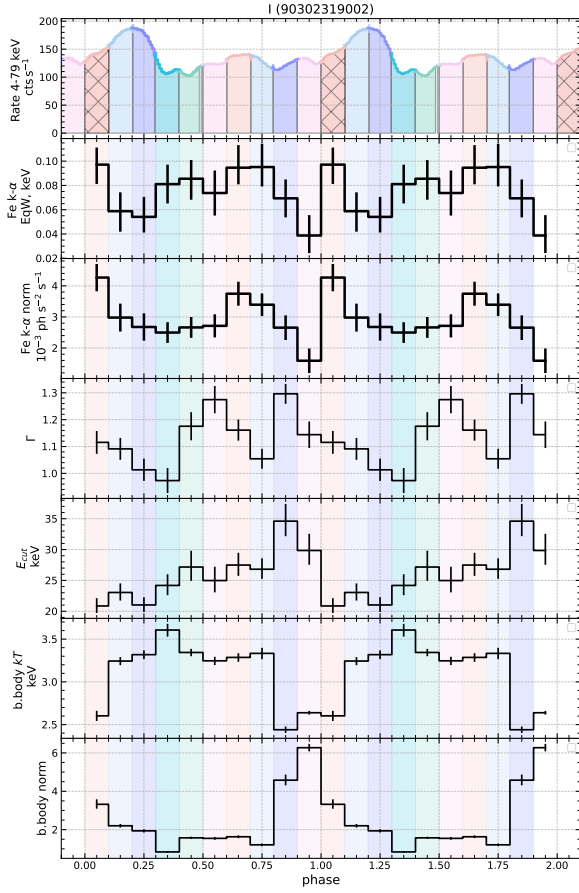
(a) Observation I, low state (edge is not included in the spectra)
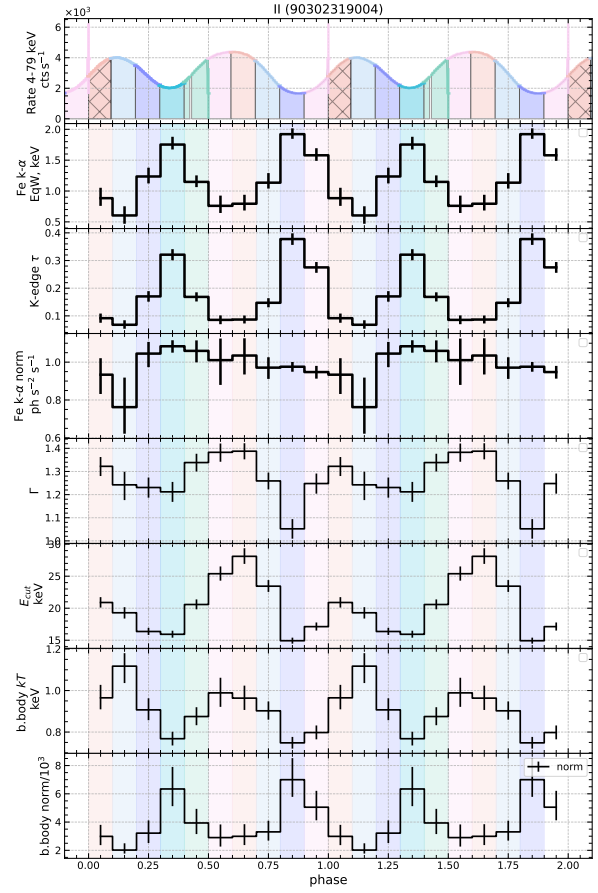
(b) Observation II, high state

Figure 4. The evolution of spectral parameters as the function of pulsar rotation phase. In each panel from top to bottom subplot: Pulse profile of the count rate in the 4-79 keV energy range; 6.4 keV Gaussian equivalent width in keV; K-edge optical depth; 6.4 keV Gaussian normalisation; Photon index of the continuum; e-folding energy of the continuum; black body inferred temperature; black body inferred normalization. Two phase intervals are plotted.

APPENDIX A: PHASE-RESOLVED PARAMETERS

APPENDIX B: COMPTT CONTINUUM MODEL

This paper has been typeset from a TEX/LATEX file prepared by the author.
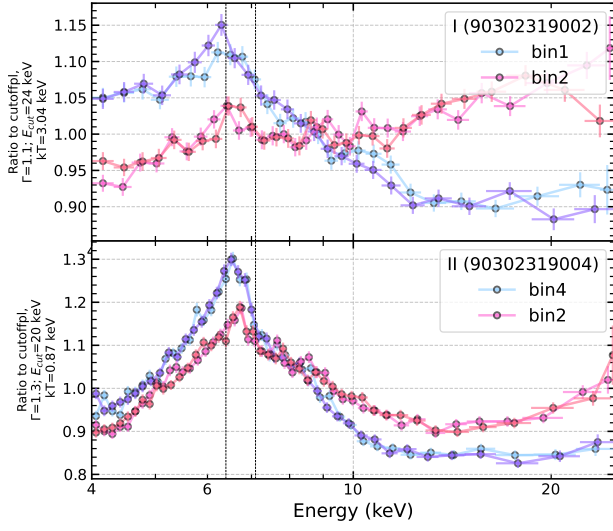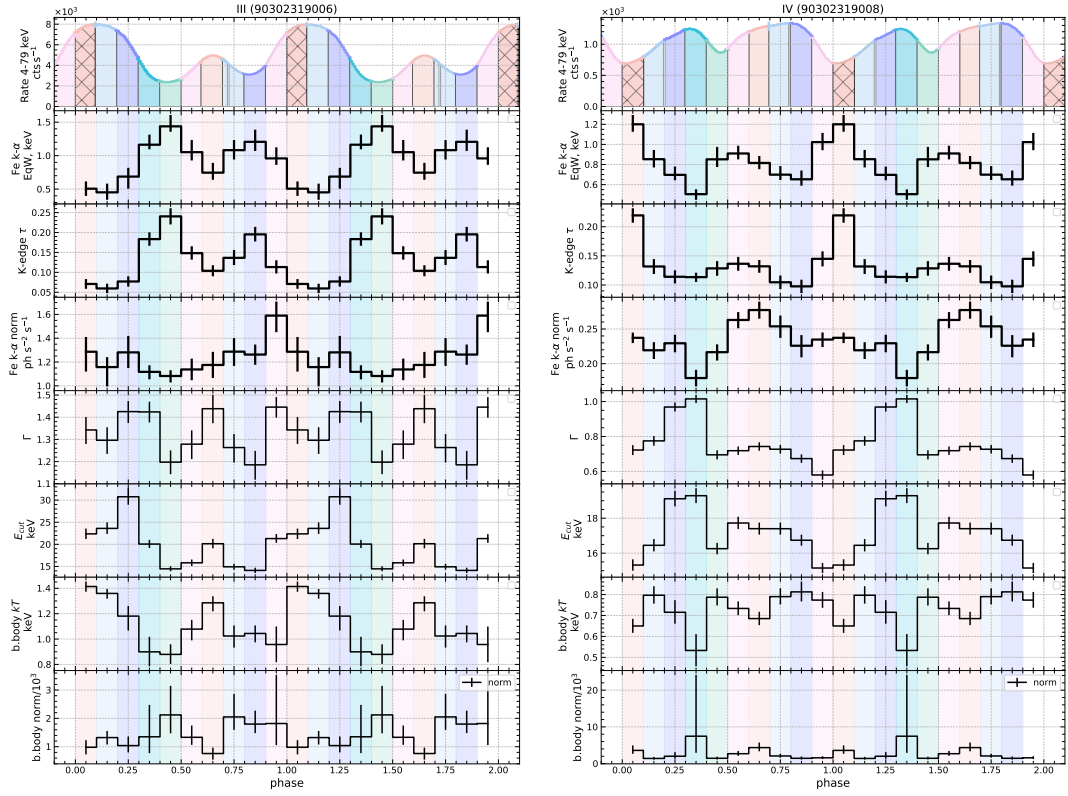
Figure 5. The ratio of the spectra collected in specified phase intervals (as indicated in the legend) to the model of cutooffpl+bbodyrad with parameters from the phase-averaged spectra. Data from both detectors are plotted in the figure. Top panel shows the results for observation I (low state), and the bottom - for observation II (high state).

(a) Observation III, high state

(b) Observation IV, high state
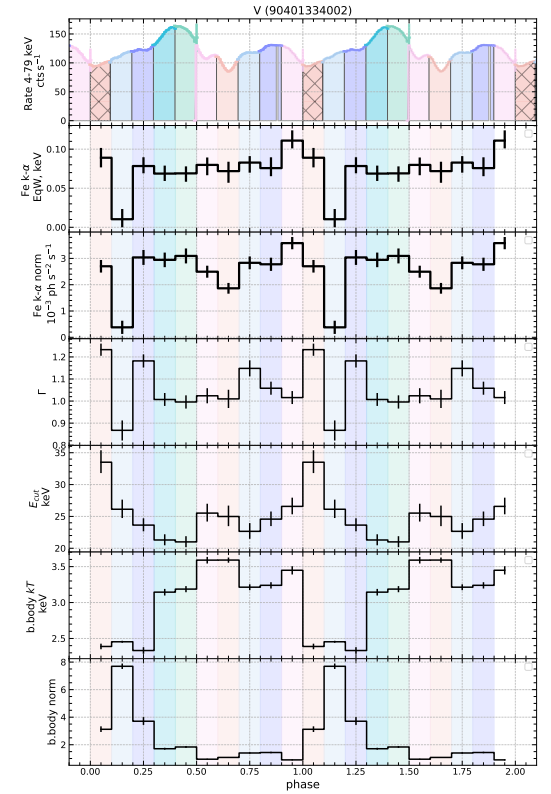
(c) Observation V, low state (edge is not included in the spectra)

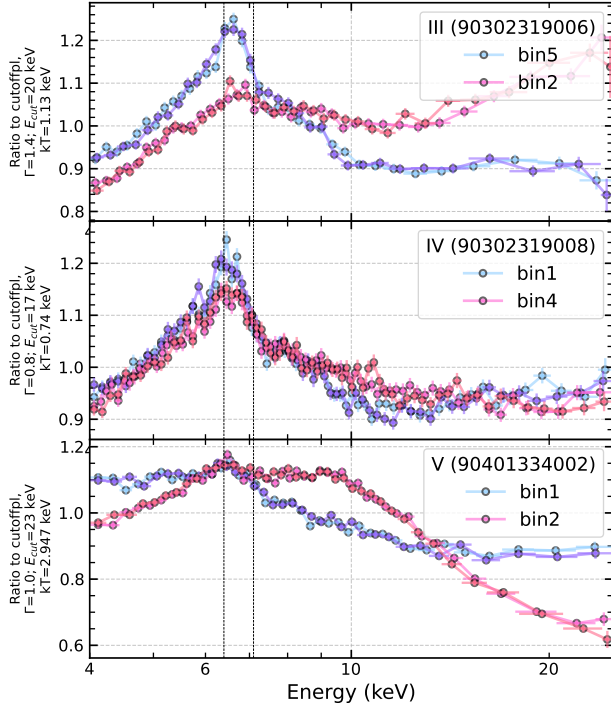**Figure A1.** As Fig. 4, but for the remaining three observations.

Figure A2. Same as Fig. 5 for observations III, IV and V.